

Atomic Depth Estimation From Noisy Electron Microscopy Data Via Deep Learning

Matan Leibovich*, Mai Tan†, Adria Marcos Morales‡, Sreyas Mohan‡, Peter A. Crozier†, Carlos Fernandez-Granda*‡

Abstract—We present a novel approach for extracting 3D atomic-level information from transmission electron microscopy (TEM) images affected by significant noise. The approach is based on formulating depth estimation as a semantic segmentation problem. We address the resulting segmentation problem by training a deep convolutional neural network to generate pixel-wise depth segmentation maps using simulated data corrupted by synthetic noise. The proposed method was applied to estimate the depth of atomic columns in CeO₂ nanoparticles from simulated images and real-world TEM data. Our experiments show that the resulting depth estimates are accurate, calibrated and robust to noise.

I. INTRODUCTION

Estimating the three-dimensional (3D) structure of objects in microscopic imaging is important for a wide-ranging array of applications. Characterizing the 3D structure of molecules is essential for the discovery of new treatments in medicine and epidemiology [1]. Determining the atomic structure of nanoparticles can provide information about their functionality, which is key to design materials with novel properties [2]. The problem is inherently complex, since imaging data is two-dimensional and often acquired under constraints that limit its signal-to-noise ratio.

In this work, we consider the problem of extracting 3D information from images obtained by transmission electron microscopy (TEM). TEM is a powerful and versatile characterization technique that is used to probe the atomic-level structure and composition of a wide range of materials, such as catalysts and semiconductors [3], [4]. Traditional estimation of 3D structures, via electron tomography, involves tilting the sample into many different orientations (typically 20 or more), recording images at each orientation, and finally reconstructing a 3D image. This approach works well for static objects, but cannot be applied to dynamic objects experiencing changes on the timescale required to record the tilt series. This situation is prevalent in material sciences when studying the functionality of materials associated with structural dynamics that occur under working conditions. Examples include the surface of a catalyst, which may change when exposed to reactants, or phase changes that occur in battery or fuel cell materials when an electrical bias is applied.

In situ electron microscopy makes it possible to probe dynamic changes in the presence of a variety of applied stimuli

[5]–[8]. To observe spatio-temporal dynamics, phase contrast imaging [9], coupled with direct electron detectors [10]–[14], now allows atomic resolution images to be recorded at more than 1000 frames per second with sub-Angstrom spatial resolution. We have recently used this approach to investigate the atomic-level changes taking place on the surface of platinum nanoparticles [15].

Motivated by the study of structural dynamics in materials, we propose *SegDepth*, a framework to estimate 3D information from individual 2D images utilizing a deep learning segmentation model. Our goal is to use TEM images to estimate the depth of the atomic columns in nanoparticles. An atomic column is a linear arrangement of atoms stacked perpendicular to the imaging plane. Estimating how many atoms are in each column is an inverse problem, which requires relating the acquired electron image intensity pattern to the underlying atomic structure. The problem is complicated by several factors, illustrated in Figure 1. First, the non-linear nature of dynamical electron scattering, underlying the phase contrast image formation processes, makes the relation between intensity and the number of atoms non-linear over realistic sample thicknesses (0 – 5 nm). Second, the signal-to-noise ratio (SNR) in the acquired time series images is extremely low, a consequence of the short exposure times required to achieve high temporal resolution and the limited electron dose rate, necessary to prevent radiation from damaging the material.

As a proof of concept for the proposed method, we focus on nanoparticles of CeO₂, a reducible oxide system with applications in catalysis, fuel cells and memristors. For such applications, there is considerable interest in understanding oxygen transport and exchange, which may manifest itself as a change in the occupancy of the oxygen atomic column in time [16]. This requires the ability to determine the oxygen column occupancy from noisy time-series data.

In order to train and evaluate the depth-estimation model, we designed a dataset of simulated TEM images of nanoparticle surfaces of varying thickness in high-symmetry zone axis orientation with respect to the incident electron beam. When the crystal is in a zone-axis orientation, peaks appear in the TEM image, representing columns of atoms in the structure. The intensity of the column is associated non-linearly with the number of atoms in the column and the depth of the column. The dataset was corrupted by Poisson noise to simulate real acquisition conditions.

As illustrated in Figure 1, we cast depth estimation as a segmentation problem, where the goal is to estimate the number of atoms or depth of the atomic column associated with each pixel in a noisy input image. Segmentation maps

*Courant Institute of Mathematical Sciences, New York University, New York, NY, USA.

†School for Engineering of Matter, Transport, and Energy, Arizona State University, Tempe, AZ, USA.

‡Center for Data Science, New York University, New York, NY, USA.

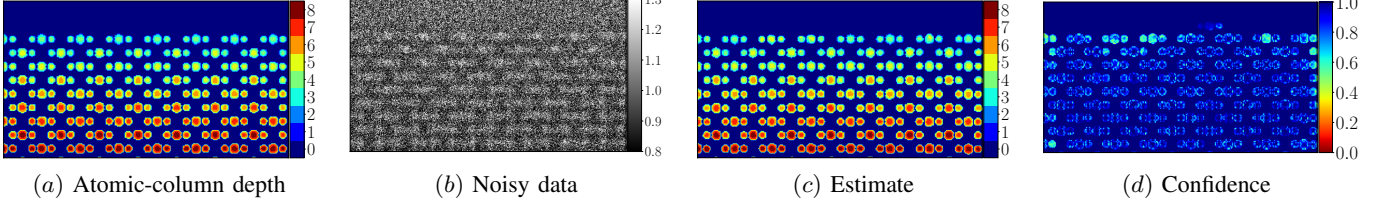


Fig. 1: **Depth estimation via segmentation.** (a) Atomic-column depth of a CeO₂ nanoparticle in (110) zone axis orientation. In this orientation the Ce and O atomic columns are distinct. The thickness of the material increases from top to bottom. (b) Noisy data generated by corrupting the TEM image corresponding to (a) with Poisson noise to simulate real acquisition data. The Ce columns in the thinner columns at the top are bright and have fainter oxygen columns to the left and right. In the thicker columns at the bottom the contrast is reversed. (c) Estimate of the atomic-column depth obtained by the proposed deep-learning based method, where a neural network is trained to approximate the depth profile (a) from the noisy data (b). (d) Confidence score of the proposed model at each pixel, computed as defined in (5), which quantifies the uncertainty in the model estimates. The confidence is generally high, except on the boundary of the nanoparticle, where estimation is more challenging.

are generated using simulated data, where the column depth is known. These masks are used to train a deep convolutional neural network, which estimates the depth from corresponding simulated noisy TEM images. The network can then be applied to real data in order to investigate the dynamics of the atomic structure of nanoparticles as they interact with the ambient environment. This framework, which we call SegDepth, is illustrated in Figure 2.

Paper outline: In **Section II** we discuss related work. In **Section III** we describe the proposed framework. In **Section IV** we provide a comprehensive evaluation of the framework using simulated data. In **Section V** we report results on real data. In **Section VI** we summarize our conclusions and outline directions for future work.

II. RELATED WORK

Deep Learning in electron microscopy: Recently, deep learning has been applied to denoise TEM images using supervised learning based on simulated data [17], [18], unsupervised learning [19], and semisupervised learning [20] (see [21] for an overview tutorial). Beyond denoising, deep neural networks have also been employed for a range of other image processing tasks in TEM [22]–[24]. For instance, [25] introduced an approach for super-resolution of TEM images, where a neural network is trained on experimentally acquired pairs of low- and high-resolution images. In the biological domain, deep learning has been applied to perform semantic segmentation of real electron microscopy images using hand-labeled training data [26], [27]. For a comprehensive overview of deep learning applications in electron microscopy see [28].

Depth estimation: Depth estimation in natural images aims to recover 3D information from their 2D projections. Early approaches estimated 3D structure from multiview images by minimizing energy-based cost functions [29] or by leveraging probabilistic priors [30]. More recently, learning-based methods have achieved state-of-the-art performance in this domain. For example, DeMoN [31] trains a neural network to estimate both motion and depth from image pairs, while DeepMVS [32] uses multiview images to predict pixel-wise depth for a reference frame. Estimating depth from a single image remains a

more difficult task, due to the inherent ambiguity in recovering continuous depth values. To address this, [33] reformulated the problem as semantic segmentation by discretizing depth into bins and training a residual CNN to predict the discretized map. Recent developments in autonomous driving have also driven interest in depth estimation as a critical component of object detection systems [34].

Depth estimation in TEM: Electron tomography consists of the acquisition of multiple TEM images from different perspectives by rotating the object, with a subsequent processing to reconstruct the whole volume. Alternatively, scanning transmission electron microscopy (STEM) and TEM images can be used to estimate 3D atomic arrangements from a single image by comparing experimental and simulated intensities. In the case of high-angle STEM modes, the incoherent nature of the image gives rise to an intensity that is proportional to the thickness and the squared atomic number, allowing more straightforward inference of depth information [35]–[37]. However, all of these techniques require the acquisition of images with a high signal-to-noise ratio (SNR) to ensure accurate estimation. In general, SNR is inversely proportional to time resolution, which means that current approaches often cannot retrieve dynamic 3D information from data acquired at high resolution.

More recently, neural networks have been employed to estimate sample thickness in high-resolution TEM data. In [38], a segmentation network was developed to determine the number of atoms per column using simulated TEM images of metal nanoparticles, showing strong performance under high electron-dose conditions. However, the model was not validated on experimental data. In [39], a regression-based network trained on simulated images was tested on real HR-TEM data of metal nanoparticles, with accuracy found to depend on the electron dose. In both studies, network performance was limited under low signal-to-noise ratio (SNR) conditions. Our application to CeO₂ nanoparticles presents additional challenges with respect to these works. The chosen crystal orientation reveals two distinct types of atomic columns: one composed of oxygen anions and the other of cerium cations. In phase contrast TEM images, these two columns

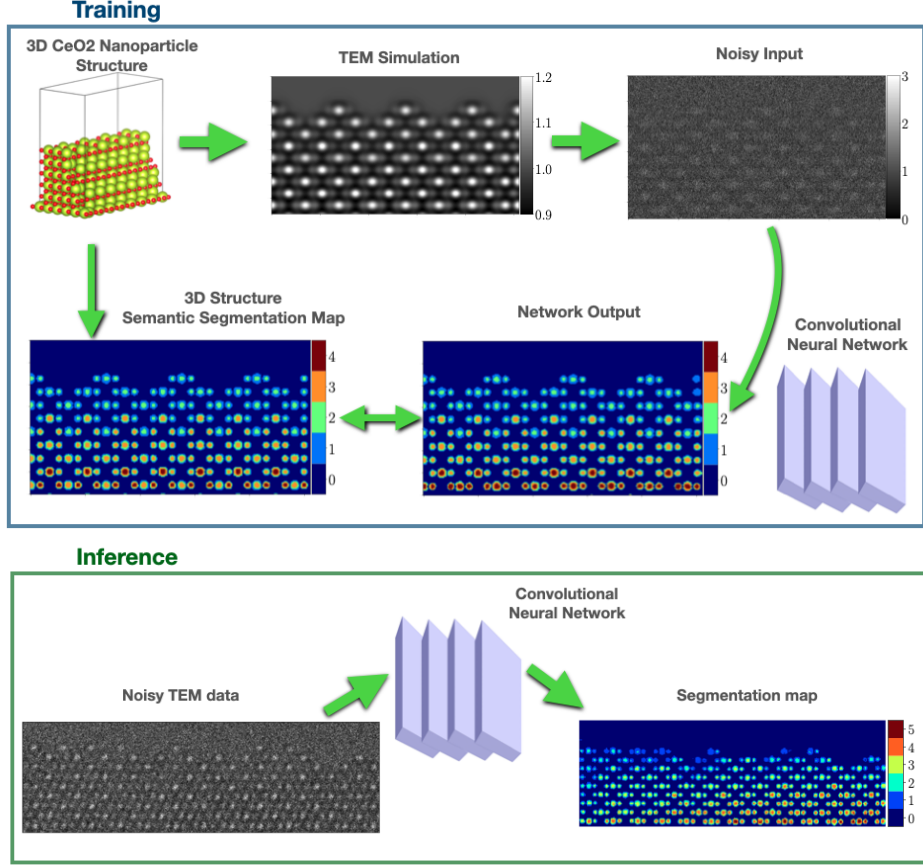


Fig. 2: **The SegDepth framework.** *Top:* A deep convolutional neural network is trained to estimate atomic-column depth using simulated data. Different 3D CeO₂ nanoparticle structures are used to generate simulated TEM data, which are then corrupted with Poisson noise to produce the noisy input to the network. The 3D structure is also used to create segmentation maps that encode the atomic-column depth. The network is trained to approximate these segmentation maps. *Bottom:* At inference, noisy TEM data is fed into the neural network to produce a segmentation map that estimates the atomic-column depth at every pixel.

have very different thickness-intensity dependencies and their occupancies may be different due to crystal thickness effects or local variations in the oxygen vacancy concentration [40]–[42].

Semantic segmentation: Our approach reformulates depth estimation as semantic segmentation. This is a fundamental problem in computer vision, where the goal is to assign labels to pixels in an image indicating what entity they correspond to [43]. In natural images, these entities are typically objects, each occupying many pixels. Semantic segmentation networks function similarly to image classifiers but operate at the pixel level, identifying regions of interest and assigning labels based on spatial and contextual features within the image domain. Recent advances, such as transformer-based detection models [44], incorporate broader contextual information to improve performance. However, the most salient features in segmentation tasks often remain dominated by localized visual cues [45].

Segmentation in the presence of noise: Semantic segmentation in the presence of noise is a critical challenge in both medical and scientific imaging applications [46]. In [47], it was proposed that jointly training a network to perform both denoising and segmentation can improve results. However,

we did not observe this in our setting; joint denoising and segmentation did not improve performance.

III. METHODOLOGY

A. The SegDepth Framework

We propose an approach to infer the depth of atomic columns of nanoparticles ordered in preferential directions from TEM images acquired from a zone axis (high-symmetry orientation). To estimate the depth, we cast this task as a semantic segmentation problem, where the labels encode the number of atoms in the atomic column corresponding to each pixel (or indicate that the pixel belongs to the background). This segmentation task is addressed by training a convolutional neural network to estimate the labels.

As depicted in Figure 2 the SegDepth neural network is trained using simulated data. Using prescribed three dimensional atomic structures, we generate synthetic TEM images and corresponding segmentation maps, encoding the column depth at every pixel. In order to mimic shot noise present in real data, the TEM images are corrupted using Poisson noise. Once trained on the synthetic data, the network can be applied to estimate depth in real TEM data.

B. Data simulation

1) *Nanoparticle atomic models*: The simulated data are based on atomic models of nanoparticles that resemble the nanoparticles in the real data of interest. In our case, we considered a cerium oxide CeO₂ (110) surface viewed along the [110] crystallographic zone axis orientation, obtained using the freely available Rhodius software [48], [49]. The surface of the atomic models have different geometric features, i.e., flat, sawtooth, or stepped shapes, previously observed in the experimental data. The average sample thickness ranged from 3 to 10 atoms. In addition, a gradual decrease in the depth of the atomic column near the surface was included, simulating the wedge structures of real nanoparticles close to their surface.

2) *TEM images*: TEM images were generated from the nanoparticle atomic models via the multi-slice approach, implemented using the Dr. Probe software package [50]. Variations in electro-optical parameters during typical TEM experiments give rise to significant modulations in the intensity of the resulting TEM images. In order to account for this, images were generated using different parameters of the electron microscope. For example, the range of the defocus value (which is critical, as it is likely to change during a real experiment) was set between 1 and 9 nm. To match the experimental data, the third order spherical aberration coefficient (C3) was set to -9 μ m resulting in white oxygen column contrast in the simulation [51], and the fifth order spherical aberration coefficient (C5) was set to be 5 mm. Lower-order aberrations were set to be 0 as those parameters are constantly tuned to be near negligible value during experiments.

We note that there are some other parameters that are less likely to be modified during a particular TEM experiment, which have been kept unchanged. For instance, images were simulated with 2048 x 2048 pixels and then down-sampled by a factor of 2 to match the approximate pixel size of the experimentally acquired image series, that is, 5.3 pm/pixel. Other aberrations, such as C3 and C5, were set to -0.009 mm and 5 mm, respectively, similar to experimental values.

3) *Noise*: The synthetic TEM images are corrupted by Poisson noise, simulating the noise produced by the behavior of low-dose electron beam. At each pixel, the value of the noisy TEM image x is generated by sampling independently from a Poisson distribution with parameter λc and scaling the result:

$$x \sim \frac{1}{\lambda} \text{Poisson}(\lambda c), \quad (1)$$

where c is the value of the clean TEM image at that pixel and λ is a parameter that determines the noise level. Since the mean and variance of a Poisson random variables are both equal to the parameter, by linearity of expectation the ratio between the mean and standard deviation of the signal at each pixel is proportional to $\sqrt{\lambda}$:

$$\frac{\mathbb{E}(x)}{\text{std}(x)} = \frac{\lambda c / \lambda}{\sqrt{\lambda c / \lambda^2}} = \sqrt{\lambda c}. \quad (2)$$

Consequently, larger values of λ correspond to higher signal-to-noise ratios.

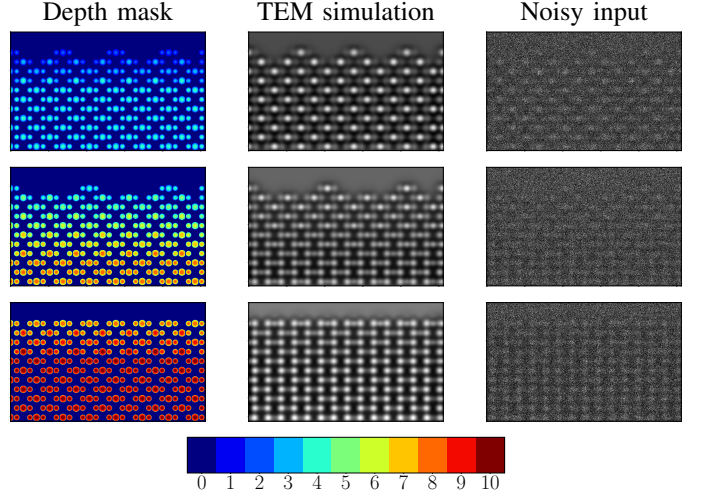


Fig. 3: **Data simulation.** Examples of simulated depth masks (left) and their associated TEM images before (center) and after (right) corrupting them with Poisson noise.

4) *Depth segmentation maps*: In order to generate the depth segmentation map associated with each TEM image, we compute the depth of the atomic column corresponding to each pixel from the three-dimensional structure of the nanoparticle atomic model used to simulate the TEM image. This is achieved by projecting each atom onto the imaging plane, and counting how many are mapped to each pixel. Examples of segmentation maps corresponding to different TEM images are shown in Figure 3. If no atoms are projected on a particular pixel, it is considered part of the background and assigned a depth of 0.

C. Deep learning

In the proposed SegDepth framework, a deep neural network is trained to estimate the segmentation maps encoding atomic-column depth from noisy TEM images. We utilize a popular architecture for image segmentation, the UNet [52], which consists of convolutional layers, as well as downsampling and upsampling layers that enable the network to capture multiscale structure. UNets have been successfully applied to denoise TEM data [21]. We follow a similar architecture to [17], which includes six downscaling layers. The architecture is described in the appendix.

The output of the UNet is fed into two downsampling layers, which produce an output with the same dimensions as the segmentation map. Then median filtering of kernel size 4 is applied to enforce similar estimates at adjacent pixels (which are more likely to belong to the same atomic column). Finally, the resulting values at each pixel are fed into a softmax layer, which generates an estimate of the probability that each pixel belongs to an atomic column with 0 to 10 atoms. Given an input image y , we denote the final output by $F_\theta(y)$, where θ represents the network parameters. For $1 \leq i \leq N$, where N is the total number of pixels in y , $F_\theta(y)_i$ is a vector of dimension 11, which approximates the probability that the atomic column

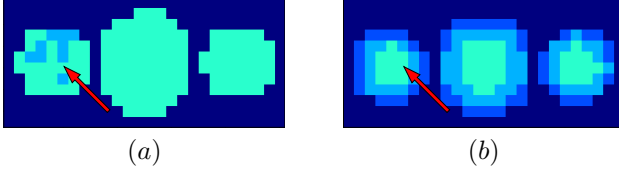


Fig. 4: **Spatial label smoothing.** (a) The pixel-wise depth segmentation labels obtained by projecting the nanoparticle atomic structure onto the imaging plane, as described in Section III-B4, contain irregular noisy patterns that change abruptly. (b) Spatial smoothing, so that the labels vary in concentric rings around each atomic column, produces more regular patterns that are easier to learn.

associated with pixel i contains each possible number of atoms (from 0 to 10):

$$\mathbb{P}(d \text{ atoms in pixel } i) \approx F_\theta(y)_i[d], \quad 0 \leq d \leq 10. \quad (3)$$

The estimated depth \hat{d}_i at the pixel i is set equal to the entry with the highest probability,

$$\hat{d}_i := \arg \max_{0 \leq d \leq 10} F_\theta(y)_i[d]. \quad (4)$$

The corresponding probability can be interpreted as the *confidence score* c_i of the model at that pixel [53], and can be used for uncertainty quantification,

$$c_i := F_\theta(y)_i[\hat{d}_i], \quad (5)$$

as illustrated in the rightmost image of Figure 1.

In order to train the network, its output is compared to a *smoothed* version of the segmentation map described in Section III-B4. As illustrated in Figure 4, the pixel-wise depth labels, computed as described in Section III-B4, contain irregular edges (e.g. changing abruptly from 0 in the background to the number of atoms in an adjacent atomic column), and can be noisy due to the projection onto the imaging plane. These patterns are difficult to learn and could result in overfitting. Consequently, we smooth the pixelwise labels, so that they decrease gradually from the atomic column to the background in concentric rings. This improves network performance and makes the interpretation of the estimated segmentation map less ambiguous.

During training, we divide the training set of clean TEM images into batches. For each fixed batch of B images $x^{[1]}, x^{[2]}, \dots, x^{[B]}$, at each training epoch we corrupt the images with noise following (1), to obtain the noisy TEM images $y^{[1]}, y^{[2]}, \dots, y^{[B]}$. Generating fresh noisy images at each epoch, a technique known as continuous noise sampling [21], prevents overfitting specific noise realizations. The network parameters are learned by minimizing a weighted cross-entropy cost function, equal to the weighted negative likelihood of the observed (smoothed) number of atoms at each pixel according to the deep neural network across the whole batch,

$$\mathcal{L}(\theta) := - \sum_{j=1}^B \sum_{i=1}^N w_{i,j} \log F_\theta(y^{[j]})_i[s_i^{[j]}] \quad (6)$$

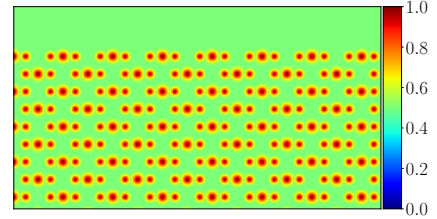


Fig. 5: **Spatial weighting to address class imbalance.** We utilize a spatial weight within the training loss in (6) to penalize misclassification in pixels that are closer to the atomic column centers. This mitigates class imbalance due to the abundance of background pixels that do not contain atomic columns.

where $s_i^{[j]}$ is the number of atoms in the i th pixel of the smoothed segmentation map corresponding to the j th TEM image in the batch.

Weighting is applied to the cross-entropy loss in (6) to address class imbalance [54], due to the fact that most of the pixels in the TEM images are background. The weight $w_{i,j}$ assigned to pixel i in image j is equal to one at the center of each atomic column and decreases gradually away from it, as illustrated in Figure 5. It penalizes misclassification of pixels belonging to atomic columns more strongly than those in the background.

In order to train the deep neural network, the loss (6) is minimized with respect to the network parameters θ via stochastic gradient descent using the Adam optimizer with learning rate scheduling [55]. The training set consists of 7×10^3 simulated TEM images and their corresponding smoothed segmentation maps. Early stopping is performed by minimizing the loss on a held-out validation dataset with 2×10^3 TEM images.

IV. EXPERIMENTS WITH SIMULATED DATA

In order to evaluate the performance of the proposed SegDepth framework, we apply it to a held out test data set of noisy TEM images paired with the corresponding ground-truth depth segmentation maps, generated as explained in Section III-B.

A. Metrics

We use the following four metrics to quantify to what extent the framework is able to recover the atomic columns and estimate their depth:

- **Pixelwise accuracy:** Fraction of pixels where the estimated depth is correct.
- **Center accuracy:** Fraction of pixels, within a neighborhood of the center of an atomic column, with radius of 16 pixels for Ce atoms and 12 pixel for O atom, where the estimated depth is correct. This metric is motivated by the fact that most pixels belong to the background, which inflates the pixelwise accuracy, whereas we are mostly interested in the pixels corresponding to atomic columns.

TABLE I: Performance of the proposed framework on the test set of simulated TEM data for different sizes of the underlying neural network model.

Base Channels	# parameters ($\times 10^6$)	Pixelwise Accuracy	Center Accuracy	Real Atom Detection Rate	Hallucinated Atom Rate ($\times 10^{-2}$)
16	11.75	0.931	0.812	0.955	7.25
32	46.92	0.932	0.842	0.944	3.58
64	18.75	0.939	0.847	0.956	2.33
96	42.17	0.936	0.83	0.943	3.62
130	77.31	0.888	0.699	0.939	1.75

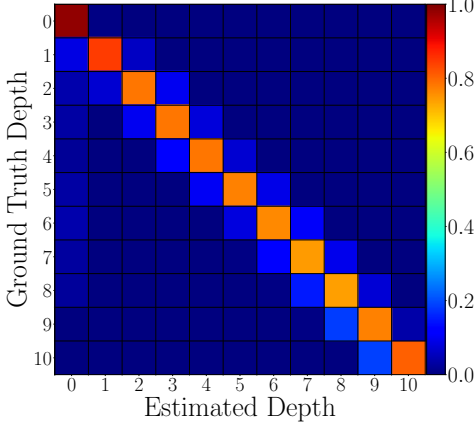


Fig. 6: **Confusion matrix.**: The confusion matrix compares the ground-truth depth and the depth estimated by the proposed framework on the test dataset of simulated TEM data, when the noise level parameter is set to 1, and the number of baseline channels equals 64. The confusion matrix is approximately diagonal, showing that the estimated depth is mostly within ± 1 atom of the ground truth depth.

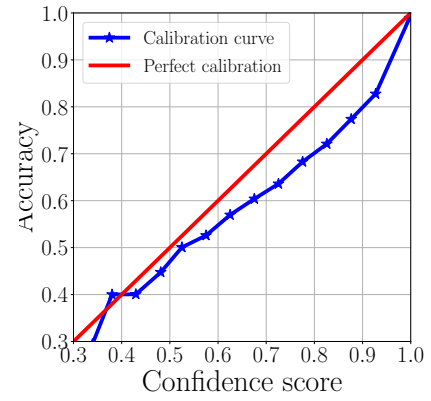


Fig. 7: **Calibration of model output.** We compare the predicted confidence score, defined in equation (5), of the proposed model (with 64 base channels) over the test set of simulated TEM images to the model accuracy, aggregated over bins of pixels with similar confidence scores. The confidence score is reasonably calibrated, the calibration curve is close to a diagonal line that would indicate perfect calibration.

- **Real atom detection rate:** Fraction of pixels belonging to atomic columns, which are detected (the estimated depth is greater than zero).
- **Hallucinated atom rate:** Fraction of pixels estimated to belong to atomic columns (the estimated depth is greater than zero), which correspond to the background.

B. Model size

Table I reports the evaluation metrics for UNet architectures with different numbers of base channels.¹ The noise parameter λ , which determines the SNR as justified by (2), is set to 2.5. The largest architecture underperforms the rest, particularly in terms of center accuracy, suggesting that it may overfit the training data to some extent. The remaining architectures achieve high pixelwise accuracy, center accuracy and real atom detection rate, while having a small hallucinated atom rate. This establishes that the framework is able to recover the underlying atomic structure from the TEM images and accurately estimate the atomic-column depths. This is confirmed by the confusion matrix in Figure 6, which shows that the majority of estimates are within one atom of the ground-truth depth.

¹In a UNet architecture the base channels are the number of channels in the first convolutional layer of the encoder. Then the number of channels doubles with each downsampling layer.

C. Calibration

Figure 7 evaluates to what extent the confidence score, defined in equation (5), is well calibrated [56], [57], in the sense that it correctly quantifies the uncertainty in the model estimate. To assess calibration we compare the predicted confidence score (computed over the test set) to the model accuracy, aggregated over bins of pixels with similar confidence scores. The confidence score is well calibrated, but tends to underestimate the uncertainty. For example, the accuracy for pixels with calibration scores close to 0.8 is around 0.7.

D. Gradient analysis

A popular approach to interpret the functions learned by deep neural networks is to compute the gradient of the output with respect to their input [21], [58], [59]. As described in Section III-C the SegDepth network utilizes a UNet that receives a TEM image as an input and outputs 11 probability maps (corresponding to the possible depth values) with the same dimensions as the input image. For each output pixel i , each possible depth value d and an input image y we can compute the gradient of the estimated probability with respect to y ,

$$g(i, d) := \nabla_y F_\theta(y)_i[d]. \quad (7)$$

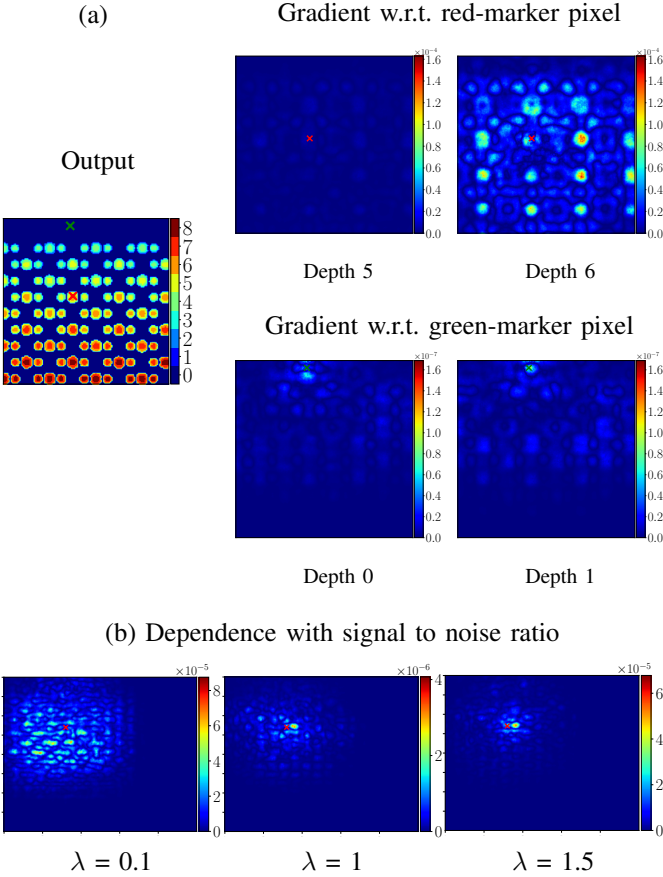


Fig. 8: Gradient visualization. The magnitude of the gradient of the neural-network output with respect to its input quantifies the sensitivity of the estimate to variations in the input pixels. (a) We consider two pixels indicated by a red and a green marker in the left image, which depicts the model output (depth estimate) for a simulated TEM image. The red marker is on an atomic column with depth 6. The magnitude of the gradient of that output pixel with respect to the input is highest for depths 5 and 6 (top right), and follows a periodic structure, which suggests that the model exploits long-range context. The green marker is in the background. The corresponding gradient magnitude is highest for depths 0 and 1 (bottom right) and is much more localized, indicating less sensitivity to long-range context. (b) Gradient magnitude of the pixel indicated by the red marker when the input to the model is the same clean TEM image corrupted using different values of the noise parameter λ . The lower the SNR, the more spread out the gradient is, indicating that the model uses longer-range context to obtain the depth estimate.

Note that here the gradient is *not* computed with respect to the network parameters θ , as during training, but rather with respect to the input image. Intuitively, the magnitude of $g(i, d)$ quantifies the sensitivity of the probability estimate for depth d at pixel i to variations in the input pixels.

In Figure 8(a) we apply this gradient analysis to two pixels, indicated by a red and a green marker, in a simulated TEM image. The red-marker pixel belongs to an atomic column with depth 6 and the green-marker belongs to the background. The

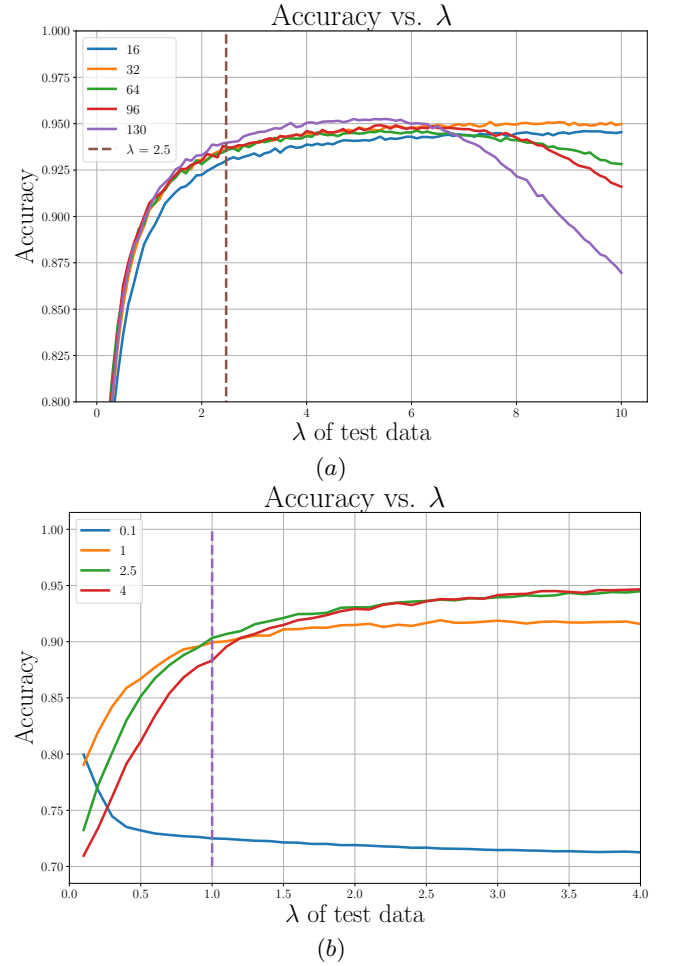


Fig. 9: Generalization to different noise levels. (a) We compare the generalization ability of models with different number of parameters when they are applied to data with different values of the noise parameter λ (horizontal axis), which determines the SNR as justified by (2). All models were trained with noisy data where λ is equal to 2.5. Models with fewer parameters generalize better to data with higher SNR. (b) We compare the generalization ability of models with 16 base channels trained using noisy data with different values of the noise parameter λ (indicated by the legend) applied to test sets generated with different values of λ (horizontal axis). Models tend to perform better close to the training noise level, generalizing well across values of λ with the same order of magnitude. However, generalization no longer occurs when λ is very different at inference and in training, as evinced by the poor generalization of the model trained with $\lambda := 0.1$.

magnitude of the gradient of both pixels with respect to the input is highest for depths close to the ground-truth (5 and 6 for the red marker, 0 and 1 for the green marker). For the background pixel, the gradient is very localized, indicating that the output is mostly sensitive to a small neighborhood around the pixel. In contrast, for the atomic-column pixel, the gradient magnitude is large at other atomic columns, suggesting that the model is able to exploit the periodic atomic structure of the nanoparticle. Figure 8(b) illustrates this phenomenon

TABLE II: Performance comparison between the proposed framework (Segmentation) and an alternative approach, where the data are first denoised and then segmented. Direct segmentation clearly outperforms two variants of this approach where the denoising and segmentation models are trained sequentially (Denoising → Segmentation) and jointly (Denoising + Segmentation). All models have 64 base channels.

Method	Pixelwise Accuracy	Center Accuracy	Real Atom Detection Rate	Hallucinated Atom Rate ($\times 10^{-2}$)
Segmentation	0.93	0.847	0.956	2.33
Denoising → Segmentation	0.867	0.765	0.946	12.35
Denoising + Segmentation	0.862	0.704	0.936	17.38

with another example, where we vary the SNR, keeping the underlying TEM image the same. At low SNR, the gradient is spread out, indicating that the model uses other atomic columns to obtain the depth estimate. As the SNR increases, the gradient becomes more localized, possibly because it is no longer necessary to rely on additional context.

E. Generalization to different noise levels

An important consideration, when evaluating neural networks designed to process real noisy data, is to what extent they generalize to different noise levels. Figure 9(a) reports the performance of several models with different number of parameters when we apply them to data with an SNR that is different from the training SNR. The models are able to generalize over a range of noise levels within an order of magnitude. Larger models tend to be less robust to changes in SNR; their performance deteriorates faster as the SNR increases beyond the training SNR. Figure 9(b) compares models that share the same architecture, but were trained at different noise levels, reporting their performance over a range of test noise levels. The models tend to perform better close to their training noise level and generalize robustly. However, performance can deteriorate dramatically at higher SNR if the training SNR is too low (as evinced by the model trained with noise parameter $\lambda := 0.1$).

F. Denoising and segmentation

In the proposed SegDepth framework, a neural network is trained to perform segmentation directly from noisy data. However, a possible alternative could be to first denoise the TEM images using a separate neural network and then perform segmentation using the denoised images. We consider two variants of this approach.

In the first variant, the denoising network is trained independently on noisy-clean pairs of TEM images in a supervised manner, minimizing the mean squared error [17], [18]. The segmentation network is then trained using the denoised TEM images and the corresponding depth segmentation maps, as described in Section III-C.

In the second variant, the denoising and segmentation networks are trained jointly. Each noisy TEM image is fed into the denoising network. The output is compared to a clean image to optimize the parameters of the denoising network. Then this output is fed into the segmentation network and the corresponding depth segmentation map is used to optimize the parameters of the segmentation network.

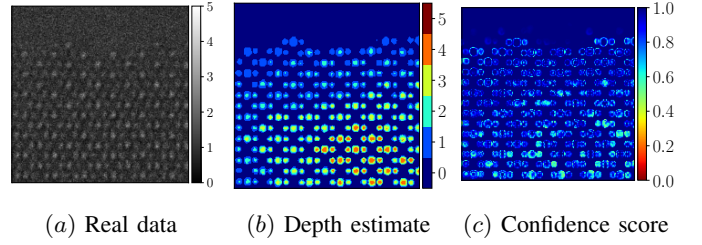


Fig. 10: **Application to real data.** (a) Real TEM image of a CeO₂ nanoparticle viewed along the [110] zone axis direction. (b) Depth estimate produced by the proposed framework SegDepth. The atomic column depth decreases towards the nanoparticle surface, which is expected. (c) Confidence score of the proposed model at each pixel, computed as defined in (5). The confidence is lower in regions where the depth estimate changes value, reflecting a greater uncertainty.

Table II shows that SegDepth outperforms both variants in all metrics. In particular, its hallucinated atom rate is much lower. The first variant which trains the two networks sequentially is better than the second, indicating that it may be challenging to jointly optimize the denoising and segmentation losses.

V. REAL EXPERIMENTAL DATA

We applied the proposed framework SegDepth to a time-resolved TEM dataset consisting of a series of images of CeO₂ catalyst (110) surfaces viewed along the [110] zone axis direction. The images were acquired using an aberration-corrected FEI Titan environmental transmission electron microscope (ETEM), operated at 300 kV and coupled with a Gatan K3 IS direct electron detector camera. The detector was operated in electron counting mode with a time resolution of 0.13 sec/frame and an incident electron dose rate of 5,000 e⁻/Å²/s. The lens system of the microscope was tuned to achieve a highly coherent parallel beam configuration with minimal low-order aberrations (e.g., astigmatism, coma), and a third-order spherical aberration coefficient of approximately -9 μm.

Although real datasets lack ground truth for evaluation, qualitative inspection of the results was promising. As illustrated in Figure 10, the depth estimate correctly identifies the positions of the atomic columns. The depth values decrease in the direction of the vacuum, which is consistent with the change in contrast between Ce and O atoms. The pixelwise confidence score, computed following (5), is mostly high, with

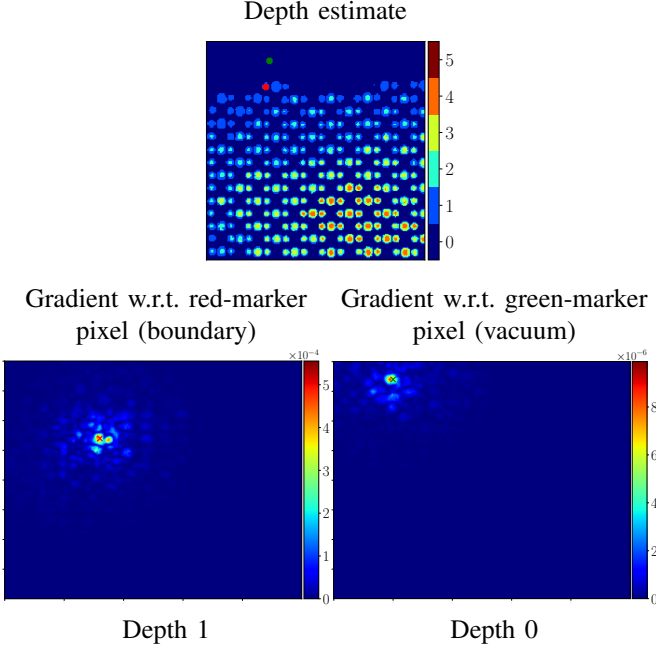


Fig. 11: Gradient analysis of real data. We apply the gradient analysis in Section IV-D to two pixels, indicated by a red and a green marker, in the TEM image from Figure 10. The red marker is at the boundary of the nanoparticle, whereas the green marker is in the vacuum. The images show the depths for which the gradient magnitude is highest: 1 for the red marker and 0 for the green marker. The gradient is mostly localized in a neighborhood of the pixels, indicating low sensitivity to long-range context at the two locations.

some lower values indicating uncertainty in transition regions, where the depth estimate changes. In Figure 11 we apply the gradient analysis in Section IV-D at two locations: the boundary of the nanoparticle and the surrounding vacuum. The gradient is mostly localized in a small neighborhood, indicating low sensitivity to long-range context.

Identifying changes in the atomic structure of nanoparticles is crucial to understand their functionality. An important application of the proposed framework is to monitor such structural dynamics. Figure 12 provides a proof of concept. The plots show the temporal evolution of the estimated depth probabilities at the two points marked in red and green in the top image of Figure 11. On the nanoparticle boundary, the estimated depth alternates between 0 and 1, indicating dynamic structural instability. At the green marker (in vacuum), the estimate is completely stable and equal to 0.

VI. CONCLUSION AND DISCUSSION

In this work we introduce a method to recover 3D atomic-scale information from noisy transmission electron microscopy (TEM) images using deep learning. The key idea is to cast depth estimation as a semantic segmentation task and train a deep convolutional neural network on simulated, noise-corrupted data to produce pixel-wise depth maps. Our results on both simulated and real TEM images suggest that this is a promising approach to obtain 3D structural information.

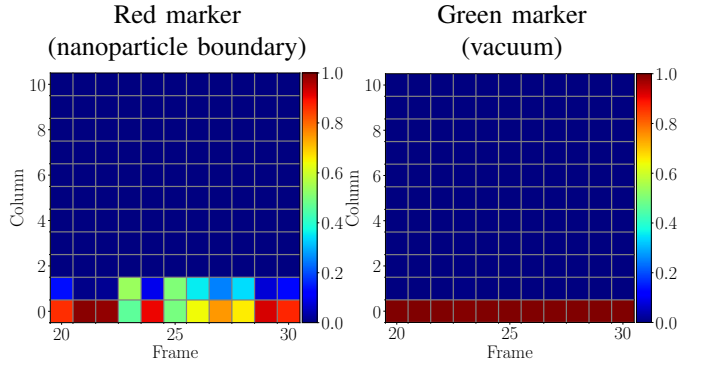


Fig. 12: Tracking structural dynamics. Applying the proposed framework at a fixed location over a period of time allows us to monitor the dynamic changes in the atomic structure of a nanoparticle. The graphs show the evolution of the probability assigned to each possible depth by the model at the two locations indicated by the red and green markers in the top image of Figure 11. On the left, the estimate at the red marker, which is at the boundary of the nanoparticle, oscillates between depths 0 and 1, identifying dynamic instability in the atomic structure. In contrast, on the right, the depth estimate at the green marker, which is in the vacuum, is constantly equal to 0.

Future work will include the creation of more sophisticated datasets that encompass diverse imaging configurations, including tilt angles, rotational variations, and scale enhancement. Similarly, it is imperative to expand the simulation datasets to include atomic defects and various elemental compositions. In addition, there is a need for further evaluation on real experimental data. Finally, from the methodological point of view, an important challenge is how to use real experimental data to train and evaluate the underlying deep-learning models, as in unsupervised [15], [19], [60]. A promising direction is to combine an unsupervised denoising loss with a supervised segmentation loss as in [61].

Acknowledgements

The authors acknowledge ASU Research Computing and NYU HPC for providing high performance computing resources, and the electron microscopes in the Eyring Materials Center at Arizona State University. We thank Joshua Vincent for providing the experimental data used in Section V. We gratefully acknowledge financial support from the National Science Foundation. NSF OAC 1940263 and 2104105 supported PAC and RM, NSF DMR 1840841 supported MT, NSF OAC 2103936 supported ML and CFG.

REFERENCES

- [1] A. Punjani, M. A. Brubaker, and D. J. Fleet, “Building proteins in a day: efficient 3d molecular structure estimation with electron cryo-microscopy,” *IEEE Transactions on Pattern Analysis and Machine Intelligence*, vol. 39, no. 4, pp. 706–718, 2016.
- [2] S. V. Kalinin, B. G. Sumpter, and R. K. Archibald, “Big–deep–smart data in imaging for guiding materials design,” *Nature materials*, vol. 14, no. 10, pp. 973–980, 2015.

[3] D. Smith, *CHAPTER 1: Characterization of nanomaterials using transmission electron microscopy*, 37th ed., ser. RSC Nanoscience and Nanotechnology. Royal Society of Chemistry, Jan. 2015, no. 37, pp. 1–29.

[4] F. Tao and P. Crozier, “Atomic-scale observations of catalyst structures under reaction conditions and during catalysis,” *Chemical Reviews*, vol. 116, no. 6, pp. 3487–3539, Mar. 2016.

[5] N. De Jonge and F. M. Ross, “Electron microscopy of specimens in liquid,” *Nature nanotechnology*, vol. 6, no. 11, pp. 695–704, 2011.

[6] M. Mecklenburg, W. A. Hubbard, E. White, R. Dhall, S. B. Cronin, S. Aloni, and B. Regan, “Nanoscale temperature mapping in operating microelectronic devices,” *Science*, vol. 347, no. 6222, pp. 629–632, 2015.

[7] T. W. Hansen and J. B. Wagner, “Controlled atmosphere transmission electron microscopy,” *Switzerland: Springer International Publishing*, pp. 213–235, 2016.

[8] F. Tao and P. A. Crozier, “Atomic-scale observations of catalyst structures under reaction conditions and during catalysis,” *Chemical reviews*, vol. 116, no. 6, pp. 3487–3539, 2016.

[9] J. C. Spence, *High-resolution electron microscopy*. OUP Oxford, 2013.

[10] G. McMullan, S. Chen, R. Henderson, and A. Faruqi, “Detective quantum efficiency of electron area detectors in electron microscopy,” *Ultramicroscopy*, vol. 109, no. 9, pp. 1126–1143, 2009.

[11] R. Clough and A. Kirkland, “Direct digital electron detectors,” in *Advances in Imaging and Electron Physics*. Elsevier, 2016, vol. 198, pp. 1–42.

[12] I. MacLaren, T. A. Macgregor, C. S. Allen, and A. I. Kirkland, “Detectors—the ongoing revolution in scanning transmission electron microscopy and why this important to material characterization,” *Appl Materials*, vol. 8, no. 11, 2020.

[13] B. Plotkin-Swing, G. J. Corbin, S. De Carlo, N. Dellby, C. Hoermann, M. V. Hoffman, T. C. Lovejoy, C. E. Meyer, A. Mittelberger, R. Pantelic *et al.*, “Hybrid pixel direct detector for electron energy loss spectroscopy,” *Ultramicroscopy*, vol. 217, p. 113067, 2020.

[14] B. D. Levin, “Direct detectors and their applications in electron microscopy for materials science,” *Journal of Physics: Materials*, vol. 4, no. 4, p. 042005, 2021.

[15] P. A. Crozier, M. Leibovich, P. Haluai, M. Tan, A. M. Thomas, J. Vincent, S. Mohan, A. Marcos Morales, S. A. Kulkarni, D. S. Matteson *et al.*, “Visualizing nanoparticle surface dynamics and instabilities enabled by deep denoising,” *Science*, vol. 387, no. 6737, pp. 949–954, 2025.

[16] A. Trovarelli and J. Llorca, “Ceria catalysts at nanoscale: how do crystal shapes shape catalysis?” *ACS catalysis*, vol. 7, no. 7, pp. 4716–4735, 2017.

[17] S. Mohan, R. Manzorro, J. L. Vincent, B. Tang, D. Y. Sheth, E. P. Simoncelli, D. S. Matteson, P. A. Crozier, and C. Fernandez-Granda, “Deep denoising for scientific discovery: A case study in electron microscopy,” *IEEE Transactions on Computational Imaging*, vol. 8, pp. 585–597, 2022.

[18] J. L. Vincent, R. Manzorro, S. Mohan, B. Tang, D. Y. Sheth, E. P. Simoncelli, D. S. Matteson, C. Fernandez-Granda, and P. A. Crozier, “Developing and evaluating deep neural network-based denoising for nanoparticle tem images with ultra-low signal-to-noise,” *Microscopy and Microanalysis*, vol. 27, no. 6, pp. 1431–1447, 2021.

[19] D. Y. Sheth, S. Mohan, J. L. Vincent, R. Manzorro, P. A. Crozier, M. M. Khapra, E. P. Simoncelli, and C. Fernandez-Granda, “Unsupervised deep video denoising,” in *Proceedings of the IEEE/CVF international conference on computer vision*, 2021, pp. 1759–1768.

[20] S. Mohan, J. L. Vincent, R. Manzorro, P. Crozier, C. Fernandez-Granda, and E. Simoncelli, “Adaptive denoising via gaittuning,” *Advances in neural information processing systems*, vol. 34, pp. 23 727–23 740, 2021.

[21] S. Mohan, K. Liu, P. A. Crozier, and C. Fernandez-Granda, “Learn, denoise, and discover: A guide to deep denoising with an application to electron microscopy,” *IEEE Signal Processing Magazine*, vol. 42, no. 2, pp. 38–56, 2025.

[22] S. Muto and M. Shiga, “Application of machine learning techniques to electron microscopic/spectroscopic image data analysis,” *Microscopy*, vol. 69, no. 2, pp. 110–122, 2020.

[23] S. R. Spurgeon, C. Ophus, L. Jones, A. Petford-Long, S. V. Kalinin, M. J. Olszta, R. E. Dunin-Borkowski, N. Salmon, K. Hattar, W.-C. D. Yang *et al.*, “Towards data-driven next-generation transmission electron microscopy,” *Nature materials*, vol. 20, no. 3, pp. 274–279, 2021.

[24] R. Lin, R. Zhang, C. Wang, X.-Q. Yang, and H. L. Xin, “Temimagenet training library and atomsegnet deep-learning models for high-precision atom segmentation, localization, denoising, and deblurring of atomic-resolution images,” *Scientific reports*, vol. 11, no. 1, p. 5386, 2021.

[25] A. Suveer, A. Gupta, G. Kylberg, and I.-M. Sintorn, “Super-resolution reconstruction of transmission electron microscopy images using deep learning,” in *2019 IEEE 16th International Symposium on Biomedical Imaging (ISBI 2019)*. IEEE, 2019, pp. 548–551.

[26] A. Khadangi, T. Boudier, and V. Rajagopal, “Em-stellar: benchmarking deep learning for electron microscopy image segmentation,” *bioRxiv*, 2020.

[27] J. Roels and Y. Saeys, “Cost-efficient segmentation of electron microscopy images using active learning,” *arXiv preprint arXiv:1911.05548*, 2019.

[28] J. M. Ede, “Deep learning in electron microscopy,” *Machine Learning: Science and Technology*, 2020.

[29] R. A. Newcombe, S. J. Lovegrove, and A. J. Davison, “Dtam: Dense tracking and mapping in real-time,” in *2011 international conference on computer vision*. IEEE, 2011, pp. 2320–2327.

[30] M. Pizzoli, C. Forster, and D. Scaramuzza, “Remode: Probabilistic, monocular dense reconstruction in real time,” in *2014 IEEE International Conference on Robotics and Automation (ICRA)*. IEEE, 2014, pp. 2609–2616.

[31] B. Ummenhofer, H. Zhou, J. Uhrig, N. Mayer, E. Ilg, A. Dosovitskiy, and T. Brox, “Demon: Depth and motion network for learning monocular stereo,” in *Proceedings of the IEEE conference on computer vision and pattern recognition*, 2017, pp. 5038–5047.

[32] P.-H. Huang, K. Matzen, J. Kopf, N. Ahuja, and J.-B. Huang, “Deepmvs: Learning multi-view stereopsis,” in *Proceedings of the IEEE Conference on Computer Vision and Pattern Recognition*, 2018, pp. 2821–2830.

[33] Y. Cao, Z. Wu, and C. Shen, “Estimating depth from monocular images as classification using deep fully convolutional residual networks,” *IEEE Transactions on Circuits and Systems for Video Technology*, vol. 28, no. 11, pp. 3174–3182, 2017.

[34] K. Park, S. Kim, and K. Sohn, “High-precision depth estimation with the 3d lidar and stereo fusion,” in *2018 IEEE International Conference on Robotics and Automation (ICRA)*. IEEE, 2018, pp. 2156–2163.

[35] R. Xu, C.-C. Chen, L. Wu, M. Scott, W. Theis, C. Ophus, M. Bartels, Y. Yang, H. Ramezani-Dakhel, M. R. Sawaya *et al.*, “Three-dimensional coordinates of individual atoms in materials revealed by electron tomography,” *Nature materials*, vol. 14, no. 11, pp. 1099–1103, 2015.

[36] E. Padgett, N. Andrejevic, Z. Liu, A. Kongkanand, W. Gu, K. Moriyama, Y. Jiang, S. Kumaraguru, T. E. Moylan, R. Kukreja *et al.*, “Connecting fuel cell catalyst nanostructure and accessibility using quantitative cryo-stem tomography,” *Journal of The Electrochemical Society*, vol. 165, no. 3, pp. F173–F180, 2018.

[37] J. Zhou, Y. Yang, Y. Yang, D. S. Kim, A. Yuan, X. Tian, C. Ophus, F. Sun, A. K. Schmid, M. Nathanson *et al.*, “Observing crystal nucleation in four dimensions using atomic electron tomography,” *Nature*, vol. 570, no. 7762, pp. 500–503, 2019.

[38] J. Madsen, P. Liu, J. Kling, J. B. Wagner, T. W. Hansen, O. Winther, and J. Schiøtz, “A deep learning approach to identify local structures in atomic-resolution transmission electron microscopy images,” *Advanced Theory and Simulations*, vol. 1, no. 8, p. 1800037, 2018.

[39] M. Ragone, V. Yurkiv, B. Song, A. Ramsubramanian, R. Shahbazian-Yassar, and F. Mashayek, “Atomic column heights detection in metallic nanoparticles using deep convolutional learning,” *Computational Materials Science*, vol. 180, p. 109722, 2020.

[40] P. A. Crozier, R. Wang, and R. Sharma, “In situ environmental tem studies of dynamic changes in cerium-based oxides nanoparticles during redox processes,” *Ultramicroscopy*, vol. 108, no. 11, pp. 1432–1440, 2008.

[41] R. Wang, P. A. Crozier, and R. Sharma, “Structural transformation in ceria nanoparticles during redox processes,” *The Journal of Physical Chemistry C*, vol. 113, no. 14, pp. 5700–5704, 2009.

[42] R. Wang, P. A. Crozier, R. Sharma, and J. B. Adams, “Measuring the redox activity of individual catalytic nanoparticles in cerium-based oxides,” *Nano letters*, vol. 8, no. 3, pp. 962–967, 2008.

[43] A. Garcia-Garcia, S. Orts-Escolano, S. Oprea, V. Villena-Martinez, and J. Garcia-Rodriguez, “A review on deep learning techniques applied to semantic segmentation,” *arXiv preprint arXiv:1704.06857*, 2017.

[44] N. Carion, F. Massa, G. Synnaeve, N. Usunier, A. Kirillov, and S. Zagoruyko, “End-to-end object detection with transformers,” in *European conference on computer vision*. Springer, 2020, pp. 213–229.

[45] K. Vinogradova, A. Dibrov, and G. Myers, “Towards interpretable semantic segmentation via gradient-weighted class activation mapping (student abstract),” in *Proceedings of the AAAI Conference on Artificial Intelligence*, vol. 34, no. 10, 2020, pp. 13 943–13 944.

[46] S. Asgari Taghanaki, K. Abhishek, J. P. Cohen, J. Cohen-Adad, and G. Hamarneh, “Deep semantic segmentation of natural and medical

images: a review,” *Artificial Intelligence Review*, vol. 54, no. 1, pp. 137–178, 2021.

[47] T.-O. Buchholz, M. Prakash, D. Schmidt, A. Krull, and F. Jug, “De-noiseg: joint denoising and segmentation,” in *European Conference on Computer Vision*. Springer, 2020, pp. 324–337.

[48] J. T.-U. Pérez-Omil, “Rhodius,” 2018, <http://www.uca.es/tem-uca>.

[49] S. Bernal, F. Botana, J. Calvino, C. López-Cartes, J. Pérez-Omil, and J. Rodriguez-Izquierdo, “The interpretation of hrem images of supported metal catalysts using image simulation: profile view images,” *Ultramicroscopy*, vol. 72, no. 3-4, pp. 135–164, 1998.

[50] J. Barthel, “Dr. probe: A software for high-resolution stem image simulation,” *Ultramicroscopy*, vol. 193, pp. 1–11, 2018.

[51] K. W. Urban, C.-L. Jia, L. Houben, M. Lentzen, S.-B. Mi, and K. Tillmann, “Negative spherical aberration ultrahigh-resolution imaging in corrected transmission electron microscopy,” *Philosophical Transactions of the Royal Society A: Mathematical, Physical and Engineering Sciences*, vol. 367, no. 1903, pp. 3735–3753, 2009.

[52] O. Ronneberger, P. Fischer, and T. Brox, “U-net: Convolutional networks for biomedical image segmentation,” in *International Conference on Medical image computing and computer-assisted intervention*. Springer, 2015, pp. 234–241.

[53] D. Hendrycks and K. Gimpel, “A baseline for detecting misclassified and out-of-distribution examples in neural networks,” *arXiv preprint arXiv:1610.02136*, 2016.

[54] M. Buda, A. Maki, and M. A. Mazurowski, “A systematic study of the class imbalance problem in convolutional neural networks,” *Neural Networks*, vol. 106, pp. 249–259, 2018.

[55] D. P. Kingma and J. Ba, “Adam: A method for stochastic optimization,” *arXiv preprint arXiv:1412.6980*, 2014.

[56] C. Guo, G. Pleiss, Y. Sun, and K. Q. Weinberger, “On calibration of modern neural networks,” in *International Conference on Machine Learning*. PMLR, 2017, pp. 1321–1330.

[57] S. Liu, A. Kaku, W. Zhu, M. Leibovich, S. Mohan, B. Yu, H. Huang, L. Zanna, N. Razavian, J. Niles-Weed *et al.*, “Deep probability estimation,” in *International Conference on Machine Learning*. PMLR, 2022, pp. 13 746–13 781.

[58] K. Simonyan, A. Vedaldi, and A. Zisserman, “Deep inside convolutional networks: Visualising image classification models and saliency maps,” *arXiv preprint arXiv:1312.6034*, 2013.

[59] S. Mohan, Z. Kadkhodaie, E. P. Simoncelli, and C. Fernandez-Granda, “Robust and interpretable blind image denoising via bias-free convolutional neural networks,” in *International Conference on Learning Representations*, 2020. [Online]. Available: <https://openreview.net/forum?id=HJISmC4FPS>

[60] A. M. Morales, M. Leibovich, S. Mohan, J. L. Vincent, P. Haluai, M. Tan, P. Crozier, and C. Fernandez-Granda, “Evaluating unsupervised denoising requires unsupervised metrics,” in *Proceedings of the 40th International Conference on Machine Learning*, 2023, pp. 23 937–23 957.

[61] T.-O. Buchholz, M. Prakash, D. Schmidt, A. Krull, and F. Jug, “De-noiseg: joint denoising and segmentation,” in *European Conference on Computer Vision*. Springer, 2020, pp. 324–337.

APPENDIX

The model is based on a U-Net convolutional encoder-decoder architecture with skip connections. The encoder path consists of an initial double-convolution block followed by a sequence of downsampling stages, each implemented as 2×2 max pooling followed by two 3×3 convolutional layers with replication padding, batch normalization, and ReLU activations. The number of resolution scales is chosen at 6, allowing the network depth and receptive field to be adjusted. At each scale, feature maps are either maintained or progressively increased in channel dimension. The number of base channels controls the fundamental width of the network and serves as the primary scaling factor for channel dimensionality throughout the architecture. The decoder mirrors the encoder, using bilinear upsampling (or optionally transposed convolutions) followed by concatenation with the corresponding encoder features and additional double-convolution blocks.

This design enables the network to combine coarse contextual information with fine spatial details through multi-resolution skip connections.

After the standard U-Net decoding path, the architecture optionally includes two additional median downsampling convolutional blocks that further process the reconstructed full-resolution features before the final output layer. These blocks reduce spatial resolution by a factor of four and increase channel dimensionality prior to a final 1×1 convolution that maps features to the desired number of output channels, corresponding to the number of possible atomic column depth values.